Chemical Engineering Journal 431 (2022) 134132

Contents lists available at ScienceDirect

Chemical Engineering Journal

journal homepage: www.elsevier.com/locate/cej

Constructing oxidized carbon spheres-based heterogeneous membrane with high surface energy for energy-free water purification

Jincui Gu [a,b], Tianyu Chen [a], Peng Xiao [a], Feng Ni [a], Luke Yan [c,*], Yujing Nie [d], Tao Chen [a,b,c,*]

[a] Key Laboratory of Marine Materials and Related Technologies, Zhejiang Key Laboratory of Marine Materials and Protective Technologies, Ningbo Institute of Material Technology and Engineering, Chinese Academy of Science, Ningbo 315201, China
[b] School of Chemical Sciences, University of Chinese Academy of Science, Beijing 100049, China
[c] Polymer Materials & Engineering Department, School of Materials Science & Engineering, Chang' an University, Xi'an 710064, China
[d] Fujian Province University Key Laboratory of Modern Analytical Science and Separation Technology, College of Chemistry, Chemical Engineering and Environment, Minnan Normal University, Zhangzhou 363000, China

ARTICLE INFO

Keywords:
Heterogeneous structure
High surface energy
Energy-free
Water purification

ABSTRACT

Producing affordable freshwater becomes increasingly essential. Membrane separation technology offers an unprecedented opportunity, but they typically use fuel energy during the separation process. Therefore, it is a severe challenge to construct an advanced membrane for energy-free water purification. Herein, for the first time, we reported a heterogeneous membrane for pressure-free water purification. Oxidized carbon spheres (OCS) membrane was optimized by the coordinated modification of polydopamine (PDA) and tetrakis(hydroxymethyl)phosphonium chloride (THPC). Remarkably, the OCS@PDA membrane was progressively hydroxylated due to the THPC's superb water-binding ability. Therefore, the OCS@PDA/THPC membrane demonstrated higher surface free energy and better hydrophilic capacity than the other membranes. Under the combined effect of abundant porous geometry and strong charge interaction, this membrane presented a splendid screening performance for various dye molecules without extra pressure. In addition, its separation throughput can be improved by regulating the external temperature. This work may offer a straightforward manner to handle the relationship between membrane structure and performance for pressure-free water purification.

1. Introduction

Freshwater scarcity has been one of the most urgent issues in human lives resulting from the booming population and increasingly severe water pollution [1–3]. Membrane separation is considered an effective technology for achieving sewage usage, benefiting from its distinctive advantages, including easy-to-tune structure, precise sieving efficiency, and low energy consumption [4–7]. To date, scientists have focused extensive interests on integrated functional membranes due to their distinct superiorities [8–13]. Numerous exciting breakthroughs in this established domain have sprung up. For instance, Xu et al. introduced a molecular bridge bearing sulfonic acid group between the adjacent nanosheets of the closely packed graphitic carbon nitride (g-C_3N_4) laminates [14]. The intercalation molecules broke up the tight interlayer distance of g-C_3N_4 laminates, giving rise to higher water permeance (~8867 L $m^{-2}h^{-1}$ bar^{-1}) than the original g-C_3N_4 membrane (~60 L $m^{-2}h^{-1}$ bar^{-1}) with a similar separation efficiency. Wang et al. fabricated a graphene-based membrane by intercalating carbon sheets into reduced graphene oxide sheets [15]. This membrane with continuous slit-shaped pores showed high efficiency for ethanol dehydration (>99.9 %) because of its tunable interlayer spacings and surface chemistry. Jiao et al. fabricated a graphene oxidized-based separation membrane with a sandwiched nanostructure through the layer-by-layer assembly. This membrane presented an excellent dye removal ability and stability [16]. Bruggen et al. fabricated a polyester-based loose membrane to achieve a low-pressure and high separation efficiency (~99.4%) for dye molecules [17]. However, during the traditional purification process, fuel energy should be supplied for these membranes to drive water molecules through the nanochannels and reject other components selectively, which aggravates the energy crisis facing modern society [18,19]. Consequently, it is pressing to construct an advanced separation membrane to achieve energy-free wastewater purification [20–24].

Specifically, the separation membranes are thermodynamically prone to form compact structures with high packing density through

* Corresponding authors.
E-mail addresses: yanlk_79@hotmail.com (L. Yan), tao.chen@nimte.ac.cn (T. Chen).

https://doi.org/10.1016/j.cej.2021.134132
Received 21 October 2021; Received in revised form 3 December 2021; Accepted 9 December 2021
Available online 14 December 2021

face-to-face aggregation, which results in the limited exposed surfaces and restricted solid–liquid interactions to remove the unwanted components effectively [25–27]. Moreover, the complex constituents in wastewater are another major obstacle the separation membranes face during water purification [28–30]. Generally, the following points should be comprehensively considered to achieve efficient pressure-free separation of the separation membranes. On the one hand, the separation membranes should endow high wettability to promote water transport [31–33]. On the other hand, the surface of the separation membranes should be smooth enough to reduce the transmission resistance of water molecules [34]. Aside from these, the surface interactions between the separation membranes and contaminations should be strong enough to facilitate the removal of target pollutants [34.35].

Carbon sphere (CS), a rich wrinkle microstructure on its surface, is favorable for water permeability [36,37]. In our preliminary work, a Janus CS-based membrane was constructed through interfacial self-assembly [38]. Under the combination of anisotropic structure and interpenetrating network, this membrane displayed ultrafast separation flux for dye molecules. Based on this, we reported the design and fabrication of oxidized carbon spheres (OCS)-based heterogeneous membrane for pressure-free wastewater purification for the first time. The designed OCS-based membrane demonstrated better hydrophilic capacity (water penetration within 0.161 s) and higher surface free energy (72.36 ± 0.11 mJ m^{-2}) than the other membranes. Under the combined effect of excellent porous geometry, an exceptional affinity for water, and the charge interaction, this membrane presented splendid screening performance for various dye molecules without pressure driving, such as Congo red with permeance up to 45.3 L $m^{-2}h^{-1}$ and rejection > 99.3%. Therefore, this OCS-based membrane presented distinct superiorities, including energy-saving, high-efficient, and a wide range of water purification. This work has provided an advanced functional separation membrane for pressure-free water purification and will shed light on designing low energy consumption environment-related materials for practical applications.

2. Experimental

2.1. Materials

Carbon spheres (CS) nanoparticles (50 ~ 70 nm) were offered by the Nafudis Technology Co., Ltd. They were the by-products during the preparation process of diamond (gas phase detonation method). Dopamine and tris(hydroxymethyl)aminomethane (Tris) and 4-dimethylaminopyridine (DMAP) were got from Sigma-Aldrich Co., Ltd. Tetrakis (hydroxymethyl)phosphonium chloride (THPC), 1-aminopyridinium iodide (1-APi) and 1-ethylpyridinium bromide ([EtPy][Br]), ethylenediamine (EDA) and diethylenetriamine (DTA) were purchased from Aladdin (Shanghai) Co., Ltd. Nylon substance with a pore size of ~ 220 nm was purchased from Millipore Industrial & Lab Chemicals. It was pre-treated with oxygen plasma under 200 Hz for 5 min. Various dye molecules, including Methyl orange (MO, 1.2 nm × 0.7 nm, 327.33 g/mol), Eriochrome black T (EBT, 1.5 nm × 0.8 nm, 461.38 g/mol), Victoria blue B (VBB, 2.1 nm × 1.9 nm, 506.08 g/mol), Acid fuchsin (AF, 1.1 nm × 1.2 nm, 585.54 g/mol), Congo red (CR, 1.3 nm × 2.8 nm, 696.66 g/mol), Brilliant blue (BB, 2.1 nm × 1.9 nm, 792.84 g/mol), Evans blue (EB, 1.3 nm × 3.1 nm, 960.81 g/mol), Alcian blue 8 (AB, 2.3 nm × 2.3 nm, 1298.86 g/mol), were got from Sigma-Aldrich Co., Ltd. These dye molecules were used without any purification. Other solvents were obtained from Aladdin (Shanghai) Co., Ltd.

2.2. Preparation of the OCS@PDA composite membrane

Firstly, CS nanoparticles (0.5 mg, 0.75 mg, 1.0 mg, 1.25 mg, 1.5 mg) were oxidized with the mixed solution of sulfuric acid and nitric acid (volume ratio = 3:1) for different days (1 ~ 6 days). Secondly, these oxidized CS nanoparticles were neutralized with sodium hydroxide solution to get the pure OCS nanoparticles. They were alternately cleaned with anhydrous ethanol and distilled water three times and dried in a vacuum oven under 30 °C for 6 h. Thirdly, the OCS nanoparticles were immersed into the dopamine solution (1 mg/ml, 1 M Tris buffer, pH = 8.5) and stirred at room temperature for 4 h. Lastly, the OCS@PDA membrane was obtained through vacuum filtration on the nylon filter paper under 0.02 Mpa and dried under 50 °C for two hours.

2.3. Preparation of the OCS@PDA/THPC composite membrane

Firstly, THPC dispersion with different concentrations was prepared by regulating the relative dosage of THPC and DMAP. In the case of the dosage ratio between THPC and DMAP being 4:1, the concentrations of THPC were 5%, 10%, 15%, 20%, 25%, 30%, 35%, respectively. Secondly, the OCS@PDA membrane was immersed into the THPC dispersion for 30 min at room temperature. Thirdly, they were placed into the vacuum oven under 40 °C two hours. Lastly, they were alternately rinsed with water and ethanol three times and then dried at 40 °C to obtain the OCS@PDA/THPC composite membrane with different THPC contents.

2.4. Preparation of OCS@PDA/1-APi and OCS@PDA/[EtPy][Br] composite membranes

The OCS@PDA/1-APi and OCS@PDA/[EtPy][Br] composite membranes were prepared for comparative experiments. Firstly, 2 g of 1-APi and [EtPy][Br] were dispersed into 8 ml of water and ultrasound for 10 min to get the 1-APi and [EtPy][Br] solutions, respectively. Secondly, the OCS@PDA membranes were immersed into the 1-APi and [EtPy][Br] solutions for 30 min at 25 °C to get the OCS@PDA/1-APi and OCS@PDA/[EtPy][Br] composite membranes, respectively. Thirdly, these membranes were placed into the vacuum oven under 40 °C for two hours. Lastly, these membranes were rinsed with water and ethanol alternately three times and dried at 40 °C to obtain the OCS@PDA/1-APi and OCS@PDA/[EtPy][Br] composite membranes, respectively.

2.5. Preparation of the OCS@PDA/EDA and OCS@PDA/DTA composite membranes

The OCS@PDA/EDA and OCS@PDA/DTA membranes were also fabricated to evaluate their separation performance. Firstly, 2 ml of EDA and DTA were dispersed into 8 ml of water and then ultrasound for 30 min to get the EDA and DTA solutions, respectively. Secondly, the OCS@PDA membranes were immersed into the EDA and DTA solutions for 30 min at 30 °C to get the EDA and DTA modified OCS@PDA membranes, respectively. Thirdly, these membranes were placed in the vacuum oven under 40 °C for two hours. Lastly, these membranes were rinsed with water and ethanol alternately three times and dried at 40 °C to obtain the OCS@PDA/EDA membrane and OCS@PDA/DTA membrane, respectively.

2.6. Characterization

The micromorphology of each membrane was recorded on the scanning electronic microscopy (SEM, Hitachi S4800, Japan). The cross-sectional images and the thickness of different membranes were carried out on the scanning electronic microscopy (SEM, Hitachi S4800, Japan). The confocal laser scanning microscope (CLSM, Zeiss LSM 700, Germany) was also used to observe the morphological images of each membrane. The samples were prepared according to the following. Firstly, the membrane was placed in a dust-free environment to ensure the accuracy of the results. Secondly, the membrane was cut into the same size membrane. Then, the membrane was treated with nitrogen to remove adsorbed impurities. These tests were carried out three times to ensure the accuracy of the data. The roughness of these membranes was recorded on the atomic force microscopy (AFM, Bruker Dimension ICON, America). Each membrane was tested three times to acquire its

accurate topography. The specific surface area of the CS and OCS nanoparticles was carried out on the micrometric surface area analyzer (ASAP 2020 M, America) for N_2 gas adsorption. Each membrane's wettability was obtained at room temperature from the contact angle measuring instrument (OCA-20, Data physics, America). Three different locations were investigated to get the average value. X-ray photoelectron spectroscopy (XPS, Thermo Fisher ESCALAB 250Xi, Japan), and Thermogravimetric analysis (TG, Perkin Elmer STA600, America) were analyzed to study the chemical constituents of each membrane, respectively. Zeta potential analyzer (Zeta, Nano ZS, England) was exploited to test the zeta potentials of each membrane. The concentration of dye molecules was monitored by a UV–vis spectrophotometer (UV–vis, Lambda 950, Japan). Noting: all tests were carried out three times to ensure accuracy. These results were obtained through multiple times tests.

3. Results and discussion

The OCS@PDA/THPC heterogeneous membrane was obtained through vacuum-assisted filtration and subsequent interface modification (Fig. 1**A**). Specially, the OCS nanoparticle was modified with dopamine mainly through multiple H-bonding. The PDA provided a platform for further functionalizing the OCS membrane, attributing to abundant phenolic hydroxyl and amino groups. In addition, the roughness of the OCS membrane can be reduced by modifying PDA, facilitating the fast transmission of water molecules. Then, the THPC was exploited in surface modification of the OCS@PDA membrane. Notably, it endows a tetrahedral molecular structure far different from the planar monomers [39]. Additionally, it possesses superb water-binding ability via multiple H-bonding [40,41]. The OCS@PDA/THPC composite membrane was uniformly assembled on the nylon substance pre-treated with O_2 plasma (**Figure S1**). The free radicals on the nylon substance can form a strong combination with the OCS@PDA/THPC composite membrane [27,38]. Even after physical destruction, it cannot fall off the substrate (**Figure S1**). This result indicated that PDA was served as a polymer bridge to make OCS@PDA/THPC membrane and nylon substance tightly combined.

Scanning electron microscopy (SEM) was carried out to characterize microstructures of CS nanoparticles before and after being oxidized. As presented in **Figure S2**, the diameter of CS nanoparticles was 53 ± 3 nm. It showed a spheroid shape with irregular wrinkles on its surface. Moreover, there was almost no apparent change in the microstructure of OCS nanoparticles. However, the CS nanoparticles' surface area enhanced from 107 m^2/g to 219 m^2/g (**Figure S3A**), accelerating the OCS dispersion in water (**Figure S2**). Thermogravimetric (TG) results also indicated that the content of the oxygen-containing functional groups increased (**Figure S3B**). The morphology of the OCS membrane, OCS@PDA membrane, and OCS@PDA/THPC membrane was further surveyed through SEM. As shown in Fig. 1**B,** the OCS nanoparticles were randomly distributed from ~ 50 nm to ~ 120 nm, and some even aggregated seriously. However, after the PDA modification, the accumulation of OCS nanoparticles gradually weakened, and the pore size of the OCS@PDA composite membrane gradually became uniform (Fig. 1**C,** **Figure S4**). This result was mainly attributed to the multiple H-

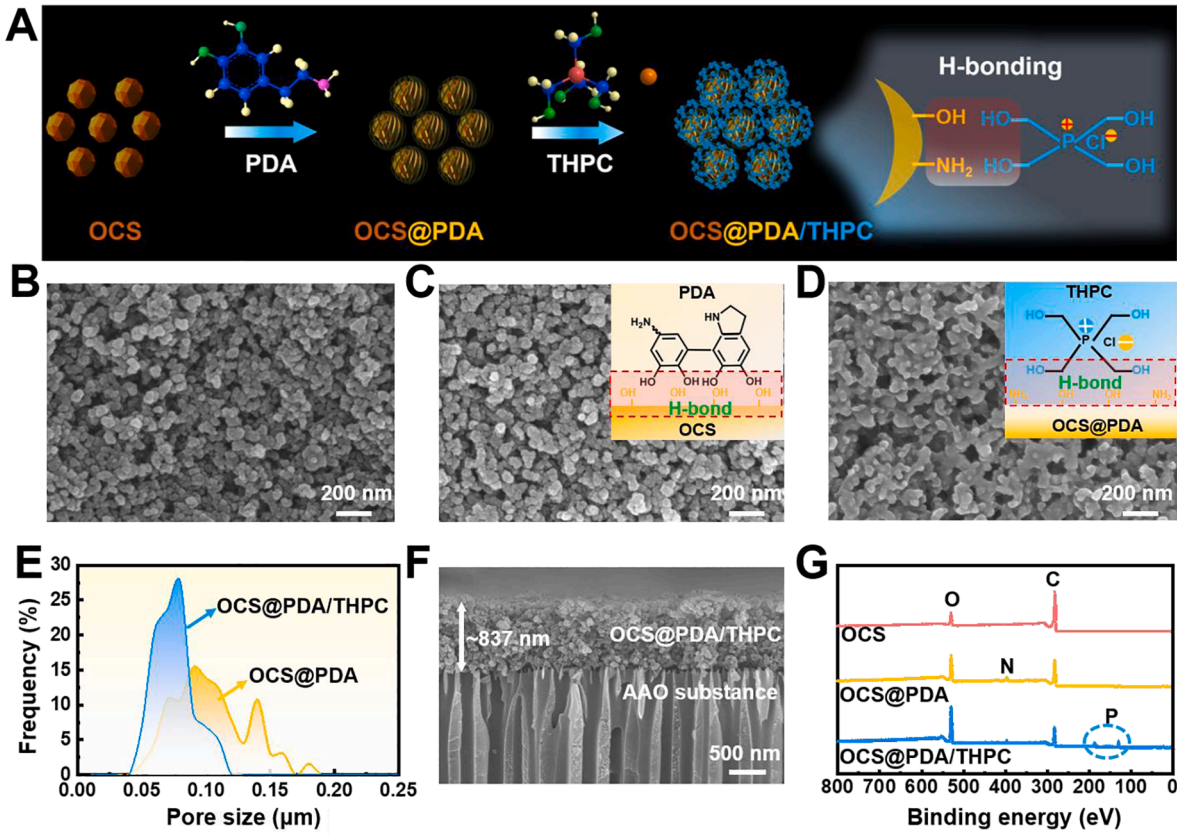

Fig. 1. (A) The schematic fabrication of the OCS@PDA/THPC composite membrane for pressure-free water purification. The blue, yellow, green, purple, red, and brown balls were carbon, hydrogen, oxygen, nitrogen, phosphorus, and chlorine atoms, respectively. (B) The SEM image of the OCS membrane. (C) The SEM image of the OCS@PDA membrane (inserting: the multiple H-bonding between the OCS particles with a large oxygen-containing functional group and PDA with phenolic hydroxyl groups and amino groups). (D) The SEM image of the OCS@PDA/THPC composite membrane (inserting: the multiple H-bonding between OCS@PDA and THPC). (E) The pore size distribution of the OCS@PDA and OCS@PDA/THPC composite membrane, respectively. (F) The cross-sectional SEM image of the OCS@PDA/THPC composite membrane (noting: AAO substance was selected to obtain clearer interface structure information). (G) XPS spectrum of the OCS, OCS@PDA, and OCS@PDA/THPC membranes, respectively.

bonding interactions between the OCS and the PDA molecules [38]. TG analysis was also carried out to calculate the mass change of the OCS membrane before and after PDA modification. As presented in **Figure S5A**, there were ~ 6.2% mass changes, indicating the PDA loss of hydrogen and oxygen atoms. In addition, the PDA molecular bridge endowed the OCS@PDA membrane an excellent mechanical strength and flexibility (**Figure S5B**).

Besides, the OCS nanoparticles' average diameter increased to ~ 100 nm after the THPC interface modification, and some OCS nanoparticles were even completely wrapped with THPC (Fig. 1**D**, **Figure S6**). Furthermore, the average pore size distribution of the OCS@PDA/THPC composite membrane concentrated from 50 nm to110 nm (Fig. 1**F**), which was smaller than that of the OCS@PDA membrane (50 ~ 180 nm). This result was due to the successful interface functionalization of the THPC. As described in Fig. 1**D**, the H-bonding can be generated among the THPC with hydroxyl functional groups and OCS@PDA membrane.

Also, the cross-section SEM images of the OCS@PDA membrane and OCS@PDA/THPC membrane were studied. As shown in **Figure S7**, it can form a compacted network among the OCS@PDA membrane with a thickness of 870 ± 26 nm. In addition, there was almost no thickness change of the OCS@PDA/THPC membrane (837 ± 32 nm) (Fig. 1**F**). Such a stacked architecture made the pores shielded by the neighboring OCS nanoparticles, minimizing the possibility of dyes penetrating through the membrane interface. Furthermore, this structure was beneficial to shorten water molecules' transmission pathways for screening performance.

X-ray photoelectron spectroscopy (XPS) was further carried out to characterize the chemical composition of the OCS membrane, OCS@PDA membrane, and OCS@PDA/THPC membrane, respectively. As displayed in **1G**, C 1 s (~298 eV) and O 1 s (~540 eV) peaks existed in these membranes [27]. **Figure S8** showed the fitted peaks of C1s at 281.2 eV, 282.3 eV, and 283.5 eV, corresponding to the C = C, C–C, and -C = O, respectively. Furthermore, there was a weak peak at ~ 398 eV in the XPS spectrum of OCS@PDA and OCS@PDA/THPC membrane, corresponding to the N 1 s in the PDA structure (Fig. 1**G**) [38]. However, the N 1 s peak almost has not existed in the OCS membrane. Three fitted peaks were observed at around 397.95 eV, 398.75 eV, 400.40 eV, assigned to the groups of C-N=, $–C_2N$-, -C-NH_2, respectively (Fig. 2**A**) [42,43]. Moreover, the content of the N element in the OCS@PDA membrane (~5.9%) was higher than that of the OCS membrane (~0.8%). This result indicated the successful interface modification of PDA. In addition, the P element can be observed at around 131 eV (P 2p) and 189 eV (P 2p) in the OCS@PDA/THPC composite membrane but not in the OCS membrane and OCS@PDA membrane, indicating the functionalization of THPC [39,44]. Also, the P 2p at the 131 eV can be divided into two peaks at 130.52 eV and 131.45 eV, corresponding to $–OCH_2$-P-H_2CO- and $–OCH_2$-P-, respectively (Fig. 2**B**). Besides, the P

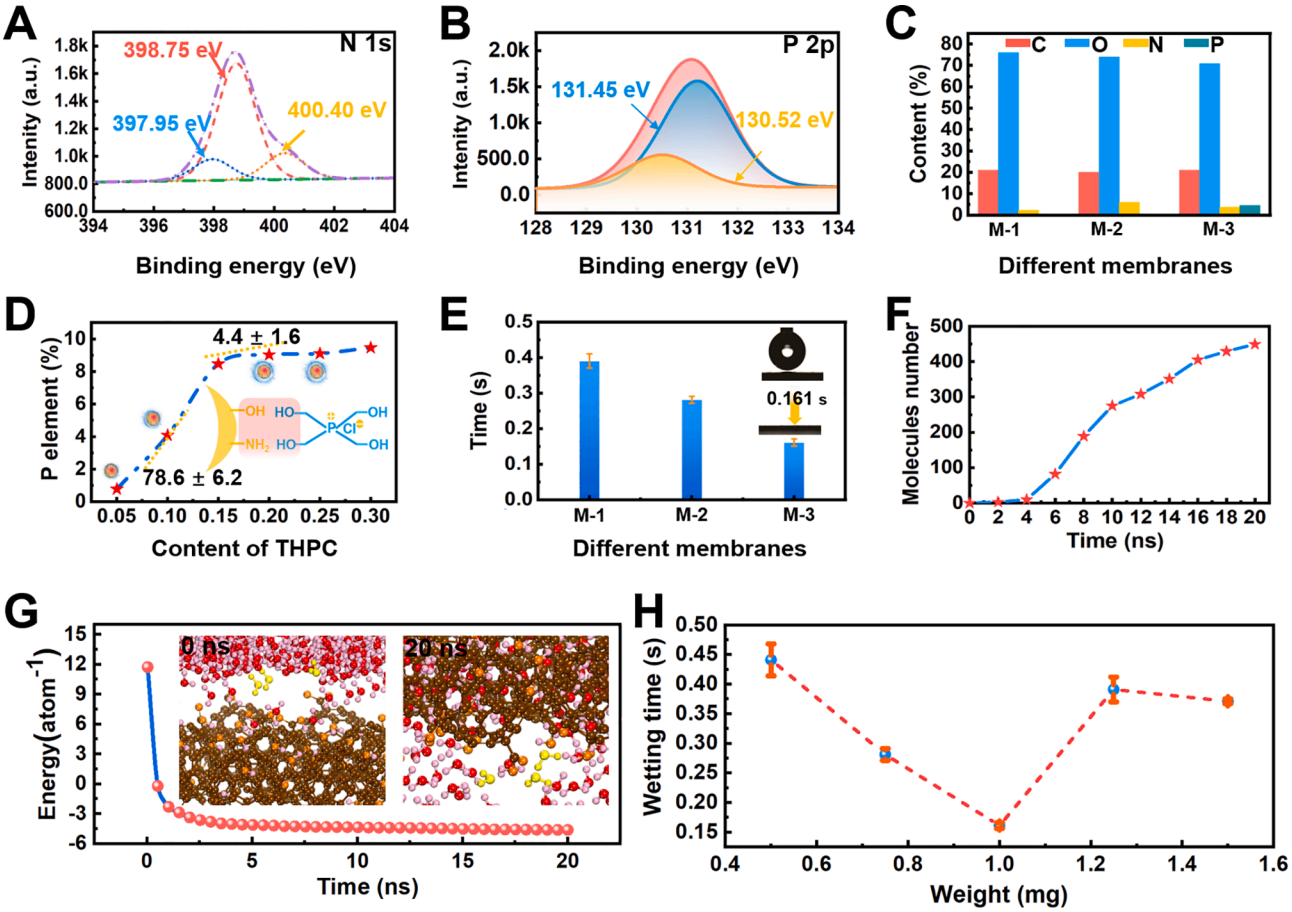

Fig. 2. (A) N1s spectrum of the OCS@PDA/THPC-20 membrane. (B) P 2p spectrum of the OCS@PDA/THPC-20 membrane. (C) The C, O, N, and P element weight contents of different membranes (M−1: OCS membrane; M−2: OCS@PDA membrane; M−3: OCS@PDA/THPC-20 membrane). (D) The P element contents along with the change of THPC concentration. (E) The wetting time of water molecules on different membranes. (Inserting: the dynamic water contact angle of the OCS@PDA/THPC-20 membrane.) (F) The MD simulation of the water transport behavior within the OCS@PDA/THPC-20 membrane. With the extension of time, the simulated permeation number of water molecules on the membrane interface increased. The transport process was not driven by external pressure. (G) The MD simulation of the total energy of the water molecule penetration process at 298 K. Insets: snapshots of the model at time frames of 5 ns. The brown, orange, pink balls were the carbon, oxygen, hydrogen atoms in the OCS@PDA/THPC-20 membrane. The red ball was the oxygen atom in the water. Some water molecules were marked in yellow to track the penetration of water molecules. (H) The wetting time of the OCS@PDA/THPC-20 membranes with different OCS weights.

element' content increased along with the addition of THPC' proportion in the OCS@PDA/THPC heterogeneous membrane. The initial P content increased fast with a slope of 78.6 ± 6.2, demonstrating the uniquely strong H-bonding between OCS@PDA and THPC. Whereas, there was only a slight change of the P element in the OCS@PDA/THPC membrane in the case of the THPC dosage ratio up to 20% with the slope of 4.4 ± 1.6 from the XPS results (Fig. 2**C-2D**). Excessive THPC brought about a severe aggregation phenomenon, not favorable for high-efficiency separation (**Figure S9**). The result from Energy dispersive spectrometer (EDS) spectrum further indicated the modification of PDA and THPC on the OCS membrane (**Figure S10**).

Water contact angle (WCA) was further carried out to investigate the wettability of these membranes and understand their interface modification process. As shown in Fig. 2**E**, the OCS membrane was superhydrophilic, and it took about 0.390 s for water (3 μL) to spread on this membrane. However, due to the hydrophilic groups of PDA molecules, the OCS@PDA membrane was more affinity to water with a penetration time of 0.281 s. Moreover, the penetration rate of water molecules within the OCS@PDA/THPC-20 membrane was faster than that of the OCS and OCS@PDA membranes. These results revealed the modification of PDA and THPC on the surface of the OCS membrane. Molecular dynamics (MD) simulation was further conducted to elaborate on water molecules' absorption, transport behavior, and recombination process within the OCS@PDA/THPC-20 composite membrane. The simulation result indicated that the water molecules could transport into the interior of the OCS@PDA/THPC-20 composite membrane within 20 ns attributing to its capillary attraction and H-bonding effect, which can stimulate more adsorption sites on this membrane for fast absorption and penetration of water molecules.

Furthermore, successive snapshots from 5 ns to 20 ns revealed the OCS@PDA/THPC-20 composite membrane's structural integrity throughout the simulation (**Figure S11**). In addition, the process and time of water passing through our structure have been evaluated using the average statistics. As shown in Fig. 2**F**, the permeation process of water molecules was slow in the initial 5 ns. However, the water molecules quickly penetrated the OCS@PDA/THPC-20 composite membrane in the mutual interaction of the capillary gravitation and exceptional absorption capacity. Furthermore, the chemical interaction between the water molecule and the OCS@PDA/THPC-20 membrane was simulated. The total energy of the water molecule penetration process decreased rapidly from ~ 11.72 eV to ~ -3.44 eV within the first 1.2 ns. It then evolved into a more stable state with the final total energy of ~ -4.62 eV per atom at 20 ns (Fig. 2**G**). Such a result revealed that the penetration of water molecules at the membrane interface was a spontaneous process. Based on the above theoretical simulation, the water molecule penetration mechanism can be proposed. The capillary force of this membrane can overcome the Vander Waals force and H-bonding among water molecules [45,46]. Moreover, the hydrophilic PDA and THPC polymer chains endowed this membrane with the exceptional absorption capacity of water molecules, which can catch the adjacent absorbed water molecules and further water molecules' recombination under the action of gravity. In this case, the water molecules can spontaneously transport from the membrane surface to its porous interior structure. The wetting behavior of the OCS@PDA/THPC-20 membrane with different OCS weights was comprehensively investigated. The surface wettability of this membrane changed distinctly. As presented in Fig. 2**H**, the hydrophilicity of the OCS@PDA/THPC-20 membrane enhanced with the increase of the content of OCS nanoparticles. The water droplets penetrated this membrane within only 0.161 s when the dosage of OCS nanoparticles approached 1.0 mg. However, it took longer for water molecules to penetrate through this membrane in case of excessive OCS nanoparticles. On the one hand, according to Wenzel mode, the OCS structure produced high roughness and increased hydrophilicity, giving rise to accelerating penetration of water droplets [47]. On the other hand, excessive OCS may cause water molecules' transmission path to becoming longer [48].

The microstructure of the OCS@PDA/THPC-20 membrane was in detail characterized through atomic force microscopy (AFM). As shown in Fig. 3**A** and **Figure S12-S13**, the roughness of the OCS membrane (214 ± 4.2 nm) was distinctly higher than that of the OCS@PDA composite membrane (130 ± 2.1 nm) and OCS@PDA/THPC-20 membrane (123 ± 3.7 nm). This difference was consistent with their responding confocal laser scanning microscope (CLSM) images (**Figure S14**). As presented in Fig. 3**B**, the OCS@PDA and OCS@PDA/THPC-20 membranes were smoother than the initial OCS membrane. The roughness reduction can facilitate the low resistance transmission of water molecules in the transmission channel inside each membrane [49]. In addition, the surface roughness of the OCS@PDA/THPC-20 membrane decreased rapidly with the extension of the oxidation time until it reached 0.30 (Fig. 3**C** and **Figure S15**). Moreover, the agglomeration of CS nanoparticles was significantly weakened by oxidation (**Figure S2**). And the roughness for CS@PDA/THPC membrane (191.3 ± 7.6 nm) was higher than the OCS@PDA/THPC-20 membrane (**Figure S16A**). Besides, the zeta potential of each membrane in different pH environments was studied in detail. As shown in Fig. 3**D**, the zeta potential of each membrane gradually changed from a lower value with the increase of pH values. The zeta potential of the OCS membrane (-17.35 ± 1.21 eV) was lower than that of the OCS@PDA membrane (-16.63 ± 1.48 eV) and OCS@PDA/THPC-20 membrane (-14.41 ± 0.06 eV) in neutral aqueous solution. These results were due to the differential functional groups in each membrane. Moreover, there was little distinction between the OCS and OCS@PDA membranes due to the similar oxygen contents in these membranes, which played a vital role in zeta potential (Fig. 2**C**). Besides, the zeta potential of the CS@PDA/THPC membrane was −20.23 ± 1.31 eV, which was lower than that of the OCS@PDA/THPC-20 membrane (Fig. 3**D**). These results were due to their differential functional groups in each membrane.

Dye molecules were applied to explore the separation performance of the OCS@PDA/THPC membrane (Fig. 4**A,** Table S1**)**. The substance showed low separation efficiency (**Figure S17A**). Furthermore, several comparative experiments were performed to obtain an advanced membrane with good rejection capacity without pressure-driven. The OCS@PDA/THPC composite membranes with different contents of THPC were prepared to achieve the maximum flux with high separation efficiency for CR solution. The penetration throughput of these membranes gradually increased along with the increase of the THPC's proportion due to the increased hydrophilicity (Fig. 4**B**).

In addition, the OCS@PDA/THPC composite membrane showed excellent rejection ability for CR solution (~99.79%) when the content of THPC was 20%. Excessive THPC (35%) can cause the OCS nanoparticles' agglomeration and bring about lower rejection ability (**Figure S11**, **Figure S17B**). The influence of the OCS' weight on the screening capacity of the OCS@PDA/THPC-20 membrane was also investigated. Along with increasing the OCS' weight, the separation flux decreased gradually, resulting from the increasing membrane' thickness (Fig. 4**C**). The rejection ability of the OCS@PDA/THPC-20 membrane reached 99.62% when the OCS' weight was 1.0 mg. Besides, proper oxidation time endowed the OCS@PDA/THPC-20 membrane with excellent retention performance (Fig. 4**D**). Based on these, the sieve performance of the OCS@PDA/THPC-20 membrane for various dye molecules was studied. As shown in Fig. 4**E**, just under gravity, the OCS@PDA/THPC-20 membrane achieved excellent separation performance for various dye molecules regardless of their space sizes and molecular weights. The penetration flux of MO, EBT, VBB, AF, CR, BB, EB, AB solutions were 45.30 ± 2.74 L $m^{-2}h^{-1}$, 30.57 ± 2.70 L $m^{-2}h^{-1}$, 40.76 ± 3.21 L $m^{-2}h^{-1}$, 38.49 ± 4.21 L $m^{-2}h^{-1}$, 44.16 ± 3.41 L $m^{-2}h^{-1}$, 39.63 ± 2.41 L $m^{-2}h^{-1}$, 36.23 ± 2.49 L $m^{-2}h^{-1}$, respectively. In addition, it presented a good rejection ability for these dye molecules with an efficiency above 98.2% (**Figure S18**). Besides, this membrane showed good cyclic separation efficiency and can withstand several harsh environments with stable separation performance for CR solution (**Figure S19**).

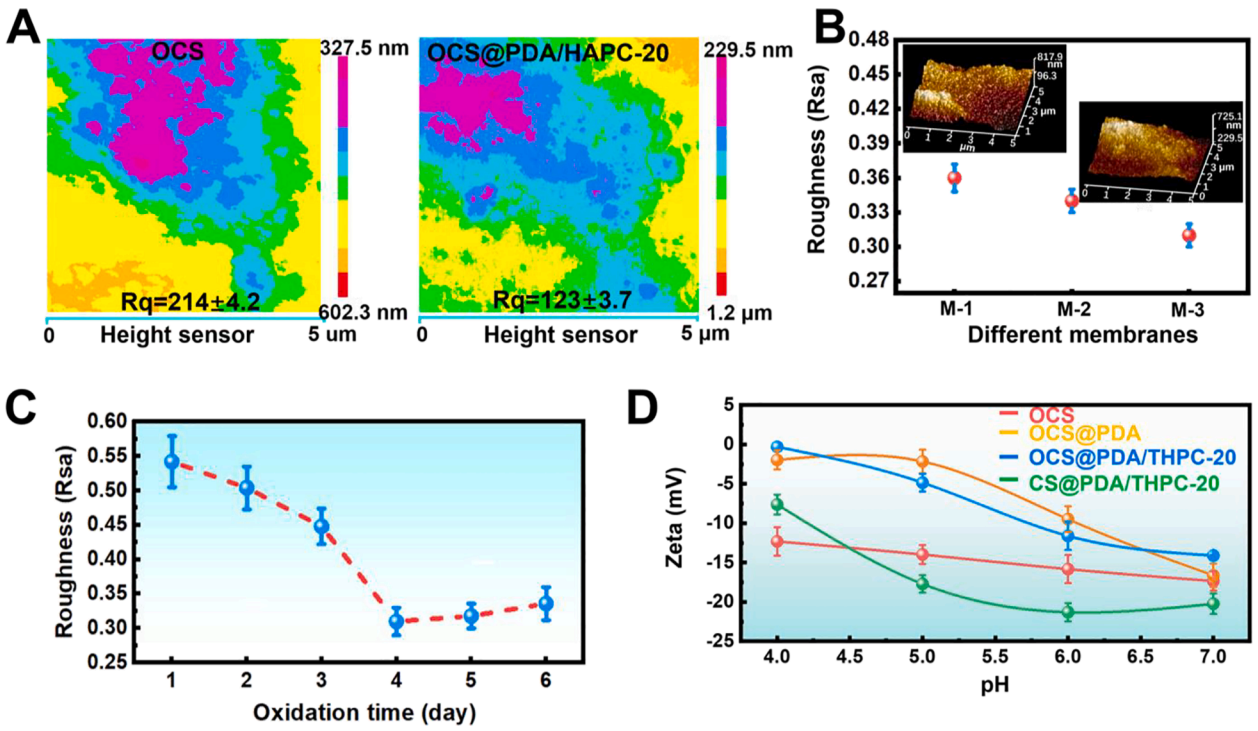

Fig. 3. (A) The AFM image results of the OCS@PDA membrane (left) and OCS@PDA/THPC-20 heterogeneous membrane (right), respectively. (B) The roughness of different membranes (M−1: OCS membrane; M−2: OCS@PDA membrane; M−3: OCS@PDA/THPC-20 heterogeneous membrane. (C) The roughness of the OCS@PDA/THPC-20 heterogeneous membrane with different oxidation times. (D) The zeta potential of different membrane under different pH environments. Noting: the content of OCS nanoparticles in the OCS@PDA/THPC-20 heterogeneous membrane was 1.0 mg.

A series of comparative membranes, including the OCS@PDA/THPC membrane (from M−1 to M−4), OCS@PDA/1-APi membrane (F-1), OCS@PDA/[EtPy][Br] membrane (F-2), OCS@PDA/DTA membrane (F-3), OCS@PDA/EDA membrane (F-4) were fabricated to explore their separation performance for CR solution systematically. Firstly, we carried out several tests to verify the successful modification of 1-APi and [EtPy][Br] on the OCS@PDA membrane (**Figure S20-S22**). As shown in Fig. 5**A**, the OCS@PDA/DTA membrane and OCS@PDA/EDA membrane had high separation flux for CR solution (72.6 ± 5.1 L $m^{-2}h^{-1}$, 63.7 ± 4.7 L $m^{-2}h^{-1}$, respectively) but weak rejection ability (~24.2% and ~ 20.1%, respectively). Moreover, the OCS@PDA/1-APi membrane and OCS@PDA/[EtPy][Br] membrane showed good separation efficiency but lower permeation flux. The apparent change in separation flux was mainly attributable to the polarity of these membranes.

Higher polarity was conducive to the rapid inside transmission of water molecules [45,46,50,51]. The surface free energy (SFE) positively correlated with the surface polarity was applied to reflect these membranes' physical characteristics indirectly [52]. The SFE of each membrane was calculated according to Owens methods [53]. As shown in Fig. 5B, the SFE enhanced with increased THPC contents in OCS@PDA/THPC membrane, attributing to the increasing polar functional groups. Therefore, the OCS@PDA/THPC-20 membrane showed higher separation flux (42.46 ± 1.21 L $m^{-2}h^{-1}$) than the OCS@PDA/THPC-15 (35.75 ± 2.97 L $m^{-2}h^{-1}$) and OCS@PDA/THPC-10 (31.46 ± 3.43 L $m^{-2}h^{-1}$) membranes. Moreover, the OCS@PDA/THPC-20 membrane endowed with higher SFE (72.36 ± 0.11 mJ m^{-2}) than the OCS@PDA/1-APi (71.68 ± 0.40 mJ m^{-2}), OCS@PDA/[EtPy][Br] (71.49 ± 0.46 mJ m^{-2}), OCS@PDA/DTA (58.93 ± 0.29 mJ m^{-2}) and OCS@PDA/EDA (62.37 ± 0.57 mJ m^{-2}) membranes (**Figure S23-S24**, Table S2). The difference was depended on the polarity and spatial molecule structure. The THPC has a higher polarity because the distance between the center of positive and negative charges of THPC (0.484 nm) was longer than that of the 1-APi (0.332 nm) and [EtPy][Br](0.305 nm). Besides, the tetrahedral structure of the THPC may provide a powerful condition for water molecules' rapid transmission (**Figure S25**). Therefore, the OCS@PDA/THPC-20 membrane possessed excellent pressure-free screening performance for water purification (Table S3-Table S4). MD simulation was performed to study the H_2O behavior of the membrane. As shown in Fig. 5**C-5D** and **Figure S26**, the OCS@PDA/THPC-20 membrane displayed higher interaction free energy (E_f) with water molecules (~1.41 kcal mol^{-1}) than the OCS@PDA/1-APi (~1.05 kcal mol^{-1}) and OCS@PDA/[EtPy][Br] (~0.59 kcal mol^{-1}) membranes, indicating its excellent water-binding capacity.

The separation throughput of the OCS@PDA/THPC-20 membrane can further be improved by regulating the external temperature. As shown in Fig. 6**A**, the OCS@PDA/THPC-20 membrane showed a more stable separation efficiency for CR solution than the OCS membrane and OCS@PDA membrane. This difference was due to the OCS@PDA/THPC-20 membrane's microstructure being denser than the other membranes. In addition, the separation flux of the OCS@PDA/THPC-20 membrane increased more rapidly than the OCS and OCS@PDA membranes. This distinguishable change was attributed to the synergistic effect of the viscosity of the feed, the temperature sensitivity of the membrane, and the surface charge effect. On the one hand, the viscosity of water molecular declined, and their thermal motion and diffusion became intense due to the increase of temperature, resulting in a much faster permeation flux during the separation process. On the other hand, Arrhenius Equation was applied to assess these membranes' permeation activation energy (E_a) [54]. As shown in Fig. 6**B** and **Figure S27**, the E_a of the OCS@PDA/THPC-20 membrane (18.71 ± 0.19 kJ mol^{-1}) was slightly higher than that of the OCS membrane (15.04 ± 0.25 kJ mol^{-1}) and OCS@PDA (16.62 ± 0.16 kJ mol^{-1}) membrane, indicating that the OCS@PDA/THPC-20 membrane was more responsive to temperature for water transport [55,56]. In addition, more dye molecules were adsorbed on the OCS membrane and OCS@PDA membrane interface but not on the OCS@PDA/THPC-20 membrane because of their differential zeta potentials. As a result, the pore size of the OCS membrane and OCS@PDA membrane may be blocked and bring out declining

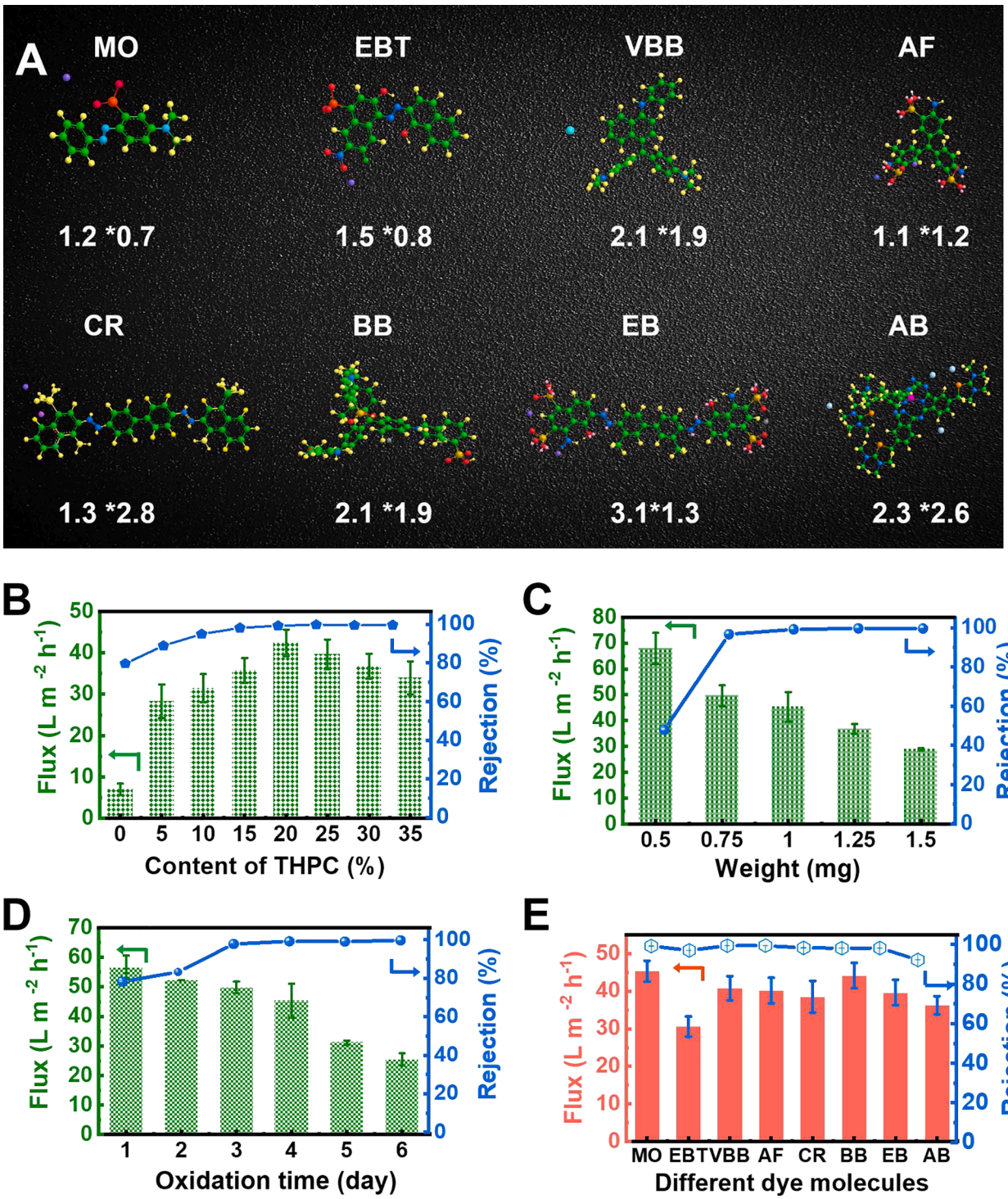

Fig. 4. (A) The spacing filling models and estimated geometric mean diameters of dye molecules. (B) The CR rejection performance of the OCS@PDA/THPC heterogeneous membrane with different THPC contents. (C) The CR rejection performance of the OCS@PDA/THPC-20 heterogeneous membrane with various CS contents. (D) The CR rejection performance of the OCS@PDA/THPC-20 heterogeneous membrane with varying oxidation times. (E) The separation performance of the OCS@PDA/THPC-20 membrane for dye molecules with different sizes and molecular weights, including MO, EBT, VBB, AF, CR, BB, EB, and AB solutions.

separation flux. Therefore, proper adjustment of the external environment can also promote the separation flux of the OCS@PDA/THPC-20 membrane.

The screening mechanism of the OCS@PDA/THPC-20 membrane was elaborated. For one thing, the rejection capacity was owing to its size screening property. The micro/nanochannels of the OCS particles were the main transmission path [57,58]. Based on the size sieving mechanism, an effective separation membrane can allow smaller particles to pass through but the larger particles to be retained. Therefore, this membrane can be applied for separating different dye molecules. For another, it was attributed to Donnan balance [59,60]. There were abundant negative charges on the OCS@PDA/THPC-20 membrane in the neutral solution (Fig. 3**D**).

Concerning cationic dyes, they were adsorbed on the surface of the OCS@PDA/THPC-20 membrane because of the electrostatic force. Under this circumstance, the cation ion concentration on the membrane

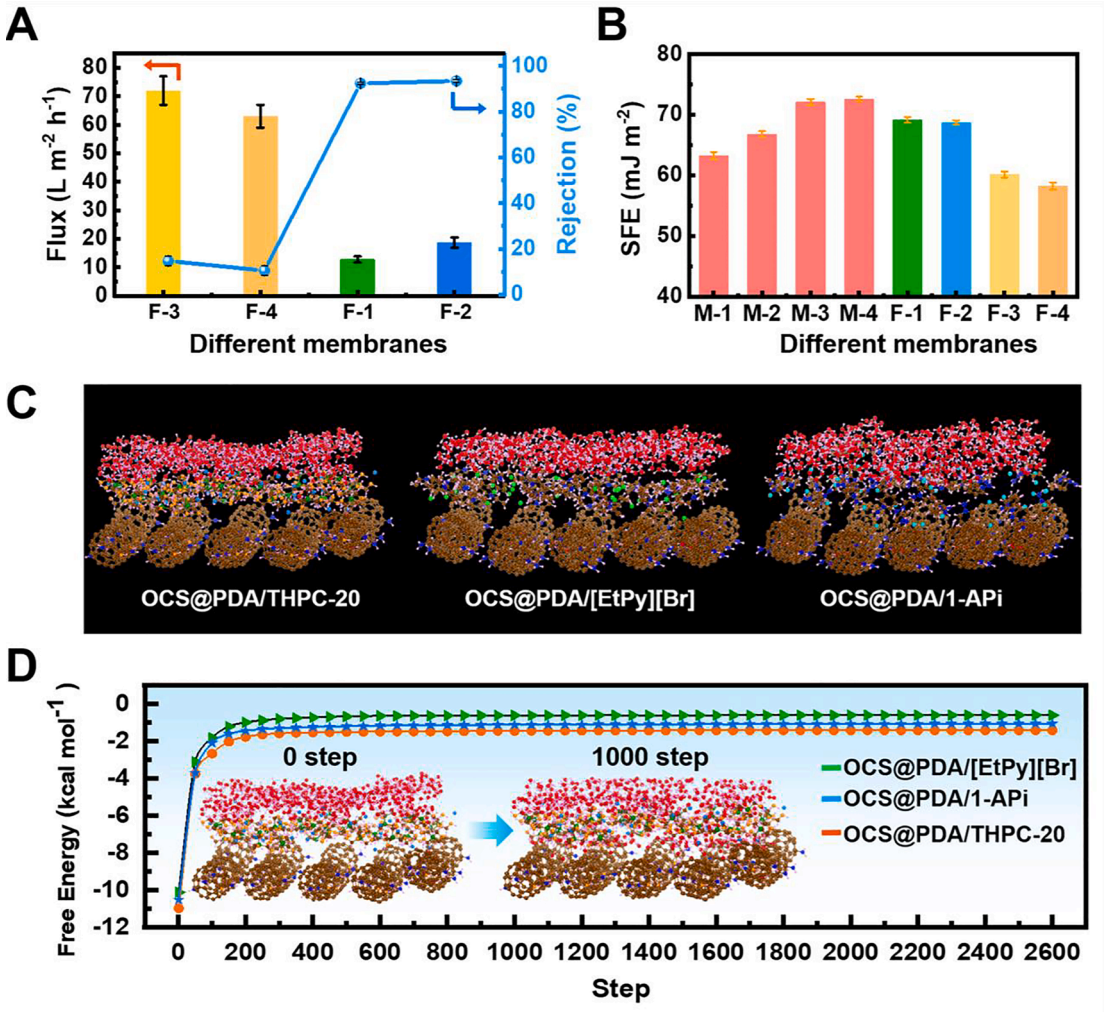

Fig. 5. (A) The rejection performance for CR solution of different membranes (F-1: OCS@PDA/[EtPy][Br]; F-2: OCS@PDA/1-APi; F-3: OCS@PDA/DTA; F-4: OCS@PDA/EDA). (B) The SFE results of different membranes (M−1: OCS@PDA/THPC-10, M−2: OCS@PDA/THPC-15; M−3: OCS@PDA/THPC-20; M−4: OCS@PDA/THPC-25). (C) MD simulation of the water molecule penetration process of the OCS@PDA/THPC-20, OCS@PDA@[EtPy][Br], and OCS@PDA@1-APi membranes, respectively. (D) MD simulation of the interaction free energies of H_2O behavior of different membranes. Inserting: the water molecule penetration process of the OCS@PDA/THPC-20 composite membrane. The brown, blue, orange, pink, dark green, light blue, light green, light blue balls were the carbon, nitrogen, oxygen, hydrogen, phosphorus, chlorine, bromine, iodine atoms, respectively. The red balls represented oxygen atoms in the water molecules.

surface was higher than that in the feed, and the concentration of anion was correspondingly lower on the surface of this membrane. The produced potential difference inhibited the transmission of anionic ions to the membrane surface to maintain charge balance. As to anionic dyes, they were blocked on the membrane surface due to the charge effect. Similarly, the cation ions were rejected to keep electrical neutrality. Therefore, the screening ability of this membrane was mainly attributed to the synergy of size effect and charge balance (Fig. 6**C**). In addition, the chemical force of water transport in the OCS@PDA/THPC-20 membrane was illustrated. Several factors, such as surface roughness, pore size distribution, chemical component, played an essential role in water molecule transport in the membrane's internal structure [60]. Therefore, the transport of water molecules was a highly complicated process. To illustrate this penetration process, the aperture of this heterogeneous membrane was modeled as a regular arrangement. As shown in Fig. 6**C**, under the effect of water molecular gravity (F_1), capillary force (F_2), and strong H-bonding derived from the THPC (F_3), this membrane can achieve efficient screening capacity for various dye molecules without external energy assistance.

4. Conclusions

Producing affordable freshwater is a severe issue that we need to address. Membrane separation technology is a practical way of taking the clean water out of wastewater. However, fuel energy should be supplied for these typical separation membranes to drive water molecules through the nanochannels and reject other components selectively, which aggravates the energy crisis facing modern society. In this work, taking advantage of CS nanoparticles and THPC, we, for the first time, designed an advanced, promising, and energy-efficient separation membrane for energy-free wastewater purification. The microstructure and wettability of the OCS-based membrane can be optimized, attributing to the interfacial functionalization of PDA and THPC. It was exciting that the designed OCS@PDA/THPC-20 membrane presented higher polarity and better water-binding ability than the other comparative membranes. Moreover, the separation throughput can be improved by regulating the external temperature due to its temperature sensitivity. Under the synergy of gravity, capillary attraction, and H-bonding, the OCS@PDA/THPC-20 membrane can achieve pressure-free and highly efficient screening performance for various dye molecules, such as CR with permeance up to 45.3 L $m^{-2}h^{-1}$ and rejection > 99.3%. In addition, it showed good cycle separation performance and harsh

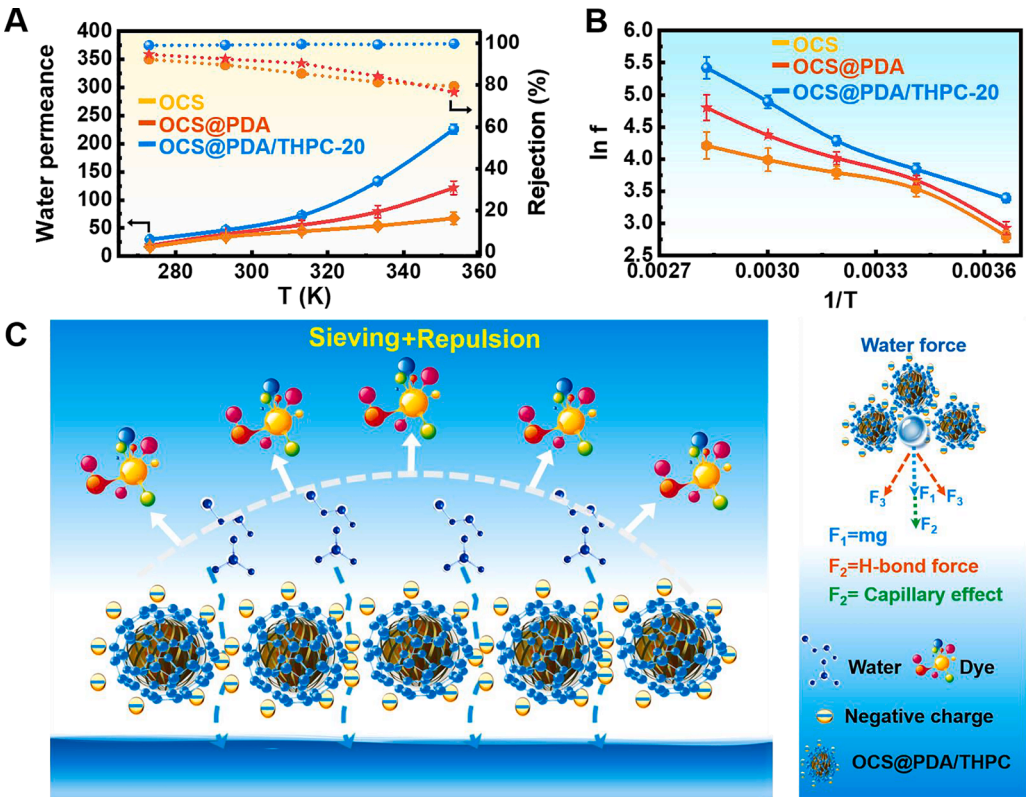

Fig. 6. (A) The separation flux of different membranes for CR solution under different temperatures. (B)The logarithmic curve relationship of the separation flux to reciprocal of the temperature of different membranes. (C) The mechanism diagram of the OCS@PDA/THPC-20 composite membrane for the rejection of dye molecules.

environmental stability. This study will provide a straightforward route to design novel functional separation membranes to directly reduce energy demand.

Declaration of Competing Interest

The authors declare that they have no known competing financial interests or personal relationships that could have appeared to influence the work reported in this paper.

Acknowledgements

We thank Jianmin Guan at the Ningbo Institute of Material Technology and Engineering, Chinese Academy of Science for his help with characterizations. This work is funded by the Public Welfare Science and Technology Projects of Ningbo (2021S150), Ningbo Science and Technology Bureau (20211ZDYF020053), K. C. Wong Education Foundation (GJTD-2019-13), the Bureau of Frontier Science and Education of Chinese Academy of Sciences (QYZDB-SSW-SLH036), the National Key Research and Development Program of China (2019YFC1606600), the Open Research Fund of Key Laboratory of Marine Materials and Related Technologies (2013DP173296, 2019K03), Special Fund for Basic Scientific Research of Central Colleges, Chang' an University (300102318403).

Appendix A. Supplementary data

Supplementary data to this article can be found online at https://doi.org/10.1016/j.cej.2021.134132.

References

[1] Y.B. Yang, X.D. Yang, L. Liang, Y.Y. Gao, H.Y. Cheng, X.M. Li, M.C. Zou, A.Y. Cao, R.Z. Ma, Q. Yuan, X.F. Duan, Large-area graphene-nanomesh/carbon-nanotube hybrid membranes for ionic and molecular nanofiltration, Science 364 (2019) 1057–1062, https://doi.org/10.1126/science.aau5321.

[2] R. Xing, W. Wang, T. Jiao, K. Ma, Q. Zhang, W. Hong, H. Qiu, J. Zhou, L. Zhang, Q. Peng, Bioinspired polydopamine sheathed nanofibers containing carboxylate graphene oxide nanosheet for high-efficient dyes scavenger, ACS Sustainable Chem. Eng. 5 (6) (2017) 4948–4956, https://doi.org/10.1021/acssuschemeng.7b0034310.1021/acssuschemeng.7b00343.s001.

[3] M. Cao, Y. Shen, Z. Yan, Q. Wei, T. Jiao, Y. Shen, Y. Han, Y. Wang, S. Wang, Y. Xia, T. Yue, Extraction-like removal of organic dyes from polluted water by the graphene oxide/PNIPAM composite system, Chem. Eng. J. 405 (2021) 126647, https://doi.org/10.1016/j.cej.2020.126647.

[4] X. Pan, S. Cheng, C. Zhang, Y. Jiao, X. Lin, W. Dong, X. Qi, Mussel-inspired magnetic pullulan hydrogels for enhancing catalytic degradation of antibiotics from biomedical wastewater, Chem. Eng. J. 409 (2021) 128203, https://doi.org/10.1016/j.cej.2020.128203.

[5] J.C. Gu, L.T. Ji, P. Xiao, C. Zhang, J. Li, L.K. Yan, T. Chen, Recent progress in superhydrophilic carbon-based composite membranes for oil/water emulsion separation, ACS Appl. Mater. Inter. 12 (13) (2021) 36679–36696, https://doi.org/10.1021/acsami.1c07737.

[6] S.Y. Cheng, X.H. Pan, C. Zhang, X.P. Lin, Q. Zhuang, Y.Z. Jiao, W. Dong, X.L. Qi, UV-assisted ultrafast construction of robust Fe_3O_4/polydopamine/Ag Fenton-like catalysts for highly efficient micropollutant decomposition, Sci. Total Environ. 26 (2021), 151182, https://doi.org/10.1016/j.scitotenv.2021.151182.

[7] C. Liu, J. Xia, J. Gu, W. Wang, Q. Liu, L. Yan, T. Chen, Multifunctional CNTs-PAA/MIL101(Fe)@Pt Composite Membrane for High-throughput Oily Wastewater Remediation, J. Hazard. Mater. 403 (2021) 123547, https://doi.org/10.1016/j.jhazmat.2020.123547.

[8] X.H. Pan, S.Y. Cheng, T. Su, G.C. Zuo, W. Zhao, X.L. Qi, W. Wei, W. Dong, Fenton-like catalyst Fe_3O_4@polydopamine-MnO_2 for enhancing removal of methylene blue in wastewater, Colloids Surf., B 181 (2019) 226–233, https://doi.org/10.1016/j.colsurfb.2019.05.048.

[9] Z. Li, X. Xu, X. Sheng, P. Lin, J. Tang, L. Pan, Y.V. Kaneti, T. Yang, Y. Yamauchi, Solar-powered sustainable water production: state-of-the-art technologies for sunlight-energy-water nexus, ACS Nano 15 (8) (2021) 12535–12566, https://doi.org/10.1021/acsnano.1c01590.

[10] F. Soyekwo, C. Liu, H. Wen, Y. Hu, Construction of an electroneutral zinc incorporated polymer network nanocomposite membrane with enhanced

selectivity for salt/dye separation, Chem. Eng. J. 380 (2020) 122560, https://doi.org/10.1016/j.cej.2019.122560.
[11] X. Qi, Q. Zeng, X. Tong, T. Su, L. Xie, K. Yuan, J. Xu, J. Shen, Polydopamine/montmorillonite-embedded pullulan hydrogels as efficient adsorbents for removing crystal violet, J. Hazard. Mater. 402 (2021) 123359, https://doi.org/10.1016/j.jhazmat.2020.123359.
[12] X. Qi, X. Tong, W. Pan, Q. Zeng, S. You, J. Shen, Recent advances in polysaccharide-based adsorbents for wastewater treatment, J. Clean. Prod. 315 (2021) 128221, https://doi.org/10.1016/j.jclepro.2021.128221.
[13] G. Zhao, H. Zhu, Cation-π interactions in graphene-containing systems for water treatment and beyond, Adv. Mater. 32 (22) (2020) 1905756, https://doi.org/10.1002/adma.v32.2210.1002/adma.201905756.
[14] J. Ran, T. Pan, Y.Y. Wu, C.Q. Chu, P. Cui, P.P. Zhang, X.Y. Ai, C.F. Fu, Z.J. Yang, T. W. Xu, Acid spacers endowing g-C_3N_4 membranes with superior permeability and stability, Angew. Chem. Int. Ed. 58 (2019) 16463–16468, https://doi.org/10.1002/anie.201908786.
[15] X. Chen, S. Mohammed, G. Yang, T. Qian, Y.u. Chen, H. Ma, Z. Xie, X. Zhang, G. P. Simon, H. Wang, Selective permeation of water through angstrom-channel graphene membranes for bioethanol concentration, Adv. Mater. 32 (33) (2020) 2002320, https://doi.org/10.1002/adma.v32.3310.1002/adma.202002320.
[16] R. Guo, T. Jiao, R. Li, Y. Chen, W. Guo, L. Zhang, J. Zhou, Q. Zhang, Q. Peng, Sandwiched Fe_3O_4/carboxylate graphene oxide nanostructures constructed by layer-by-layer assembly for highly efficient and magnetically recyclable dye removal, ACS Sustainable Chem. Eng. 6 (1) (2018) 1279–1288, https://doi.org/10.1021/acssuschemeng.7b0363510.1021/acssuschemeng.7b03635.s001.
[17] P. Jin, S. Chergaoui, J. Zheng, A. Volodine, X. Zhang, Z. Liu, P. Luis, B. Van der Bruggen, Low-pressure highly permeable polyester loose nanofiltration membranes tailored by natural carbohydrates for effective dye/salt fractionation, J. Hazard. Mater. 421 (2022) 126716, https://doi.org/10.1016/j.jhazmat.2021.126716.
[18] F. Zhu, L. Wang, B. Demir, M. An, Z.L. Wu, J. Yin, R. Xiao, Q. Zheng, J. Qian, Accelerating solar desalination in brine through ion activated hierarchically porous polyion complex hydrogels, Mater. Horiz. 7 (12) (2020) 3187–3195.
[19] Y. Guo, X. Zhao, F. Zhao, Z. Jiao, X. Zhou, G. Yu, Tailoring surface wetting states for ultrafast solar-driven water evaporation, Energy Environ. Sci. 13 (7) (2020) 2087–2095, https://doi.org/10.1039/D0EE00399A.
[20] F. Zhao, Y. Guo, X. Zhou, W. Shi, G. Yu, Materials for solar-powered water evaporation, Nat Rev Mater 5 (5) (2020) 388–401, https://doi.org/10.1038/s41578-020-0182-4.
[21] S.P. Nunes, P.Z. Culfaz-Emecen, G.Z. Ramon, T. Visser, G.H. Koops, W. Jin, M. Ulbricht, Thinking the future of membranes: Perspectives for advanced and new membrane materials and manufacturing processes, J Membrane Sci. 598 (2020) 117761, https://doi.org/10.1016/j.memsci.2019.117761.
[22] S. Cheng, C. Zhang, J. Li, X. Pan, X. Zhai, Y. Jiao, Y. Li, W. Dong, X. Qi, Highly efficient removal of antibiotic from biomedical wastewater using Fenton-like catalyst magnetic pullulan hydrogels, Carbohydr. Polym. 262 (2021) 117951, https://doi.org/10.1016/j.carbpol.2021.117951.
[23] Q. Huang, J. Chen, M. Liu, H. Huang, X. Zhang, Y. Wei, Polydopamine-based functional materials and their applications in energy, environmental, and catalytic fields: State-of-the-art review, Chem. Eng. J. 387 (2020) 124019, https://doi.org/10.1016/j.cej.2020.124019.
[24] X.Y. Zhang, Q. Huang, F.J. Deng, H.Y. Huang, Q. Wan, M.Y. Liu, Y. Wei, Mussel-inspired fabrication of functional materials and their environmental applications: progress and prospects, Appl. Mater. Today 7 (2017) 222–238, https://doi.org/10.1016/j.apmt.2017.04.001.
[25] P.L. Yap, M.J. Nine, K. Hassan, T.T. Tung, D.N.H. Tran, D. Losic, Graphene-based sorbents for multipollutants removal in water: a review of recent progress, Adv. Funct. Mater. 31 (9) (2021) 2007356, https://doi.org/10.1002/adfm.v31.910.1002/adfm.202007356.
[26] L. Yan, C. Liu, J. Xia, M. Chao, W. Wang, J. Gu, T. Chen, CNTs/TiO_2 composite membrane with adaptable wettability for on-demand oil/water separation, J. Clean. Prod. 275 (2020) 124011, https://doi.org/10.1016/j.jclepro.2020.124011.
[27] J.Y. Xia, P. Xiao, J.C. Gu, T.Y. Chen, C.H. Liu, L.K. Yan, T. Chen, Interfacial self-assembled GR/GO ultrathin membranes in large scale for molecular sieving, J. Mater. Chem. A 8 (2020) 18735, https://doi.org/10.1039/D0TA05337F.
[28] L. Ji, L. Yan, M. Chao, M. Li, J. Gu, M. Lei, Y. Zhang, X. Wang, J. Xia, T. Chen, Y. Nie, T. Chen, Sphagnum inspired g-C_3N_4 nano/microspheres with smaller bandgap in heterojunction membranes for sunlight-driven water purification, Small 17 (12) (2021) 2007122, https://doi.org/10.1002/smll.v17.1210.1002/smll.202007122.
[29] H. Wang, X. Mi, Y.i. Li, S. Zhan, 3D graphene-based macrostructures for water treatment, Adv. Mater. 32 (3) (2020) 1806843, https://doi.org/10.1002/adma.v32.310.1002/adma.201806843.
[30] Z. Liu, Z. Zhou, N. Wu, R. Zhang, B.o. Zhu, H. Jin, Y. Zhang, M. Zhu, Z. Chen, Hierarchical photothermal fabrics with low evaporation enthalpy as heliotropic evaporators for efficient, continuous, salt-free desalination, ACS Nano 15 (8) (2021) 13007–13018, https://doi.org/10.1021/acsnano.1c0190010.1021/acsnano.1c01900.s00110.1021/acsnano.1c01900.s002.
[31] D. Qi, Y. Liu, Y. Liu, Z. Liu, Y. Luo, H. Xu, X. Zhou, J. Zhang, H. Yang, W. Wang, X. Chen, Polymeric membranes with selective solution-diffusion for intercepting volatile organic compounds during solar-driven water remediation, Adv. Mater. 32 (50) (2020) 2004401, https://doi.org/10.1002/adma.v32.5010.1002/adma.202004401.
[32] Z. Wang, M. Elimelech, S. Lin, Environmental applications of interfacial materials with special wettability, Environ. Sci. Technol. 50 (5) (2016) 2132–2150, https://doi.org/10.1021/acs.est.5b04351.
[33] H.B. Zeng, K.L. Wu, X. Cui, Z.X. Chen, Wettability effect on nanoconfined water flow: Insights and perspectives, Nano Today 16 (2017) 7–8, https://doi.org/10.1016/j.nantod.2017.05.001.
[34] A. Khalil, F. Schäfer, N. Postulka, M. Stanzel, M. Biesalski, A. Andrieu-Brunsen, Wettability-defined droplet imbibition in ceramic mesopores, Nanoscale 12 (47) (2020) 24228–24236, https://doi.org/10.1039/D0NR06650H.
[35] M. Ghidiu, M.R. Lukatskaya, M.-Q. Zhao, Y. Gogotsi, M.W. Barsoum, Conductive two-dimensional titanium carbide 'clay' with high volumetric capacitance, Nature 516 (7529) (2014) 78–81, https://doi.org/10.1038/nature13970.
[36] G. Zhao, J. Li, X. Ren, C. Chen, X. Wang, Few-layered graphene oxide nanosheets as superior sorbents for heavy metal ion pollution management, Environ. Sci. Technol. 45 (24) (2011) 10454–10462, https://doi.org/10.1021/es203439v.
[37] Y.Y. Fu, Y. Liu, H. Li, Efficient coating fabrication of onion-like carbon nanoparticles via aerosol deposition, Particuology 53 (2020) 58–62, https://doi.org/10.1016/j.partic.2020.01.001.
[38] T. Chen, J. Xia, J. Gu, G. Lu, Q. Xue, C. Liu, L. Yan, T. Chen, Engineering Janus CNTs/OCS composite membrane at air/water interface for excellent dye molecules screening, Chem. Eng. J. 417 (2021) 127947, https://doi.org/10.1016/j.cej.2020.127947.
[39] H. Peng, W.-H. Zhang, W.-S. Hung, N. Wang, J. Sun, K.-R. Lee, Q.-F. An, C.-M. Liu, Q. Zhao, Phosphonium modification leads to ultrapermeable antibacterial polyamide composite membranes with unreduced thickness, Adv. Mater. 32 (23) (2020) 2001383, https://doi.org/10.1002/adma.v32.2310.1002/adma.202001383.
[40] M. Olkiewicz, M.P. Caporgno, J. Font, J. Legrand, O. Lepine, N.V. Plechkova, J. Pruvost, K.R. Seddon, C. Bengoa, A novel recovery process for lipids from microalgæ for biodiesel production using a hydrated phosphonium ionic liquid, Green Chem. 17 (5) (2015) 2813–2824, https://doi.org/10.1039/C4GC02448F.
[41] C.P. Gulka, A.C. Wong, D.W. Wright, Spontaneous self-assembly and disassembly of colloidal gold nanoparticles induced by tetrakis(hydroxymethyl) phosphonium chloride, Chem. Commun. 52 (6) (2016) 1266–1269, https://doi.org/10.1039/C5CC08211K.
[42] J.Y. Xia, J.C. Gu, P. Xiao, C. Zhang, L.K. Yan, T. Chen, Supramolecular fabrication of hyperbranched polyethyleneimine toward nanofiltration membrane for efficient wastewater purification, SusMat. (2021), https://doi.org/10.1002/sus2.33.
[43] J. Zhao, Y. Su, X. He, X. Zhao, Y. Li, R. Zhang, Z. Jiang, Dopamine composite nanofiltration membranes prepared by self-polymerization and interfacial polymerization, J. Membr. Sci. 465 (2014) 41–48.
[44] W.W. Bryan, A.C. Jamison, P. Chinwangso, S. Rittikulsittichai, T.-C. Lee, T.R. Lee, Preparation of THPC-generated silver, platinum, and palladium nanoparticles and their use in the synthesis of Ag, Pt, Pd, and Pt/Ag nanoshells, RSC Adv. 6 (72) (2016) 68150–68159, https://doi.org/10.1039/C6RA10717F.
[45] H.D. Liu, X.T. Zhang, Z.X. Hong, Z.G. Pu, Q.Y. Yao, J.C. Shi, G.B. Yang, B.W. Mi, B. Yang, X. Liu, H.F. Jiang, X.J. Hu, A bioinspired capillary-driven pump for solar vapor generation, Nano Energy 42 (2017) 115–121, https://doi.org/10.1016/j.nanoen.2017.10.039.
[46] X. Ma, Q. Liu, D.a. Xu, Y. Zhu, S. Kim, Y. Cui, L. Zhong, M. Liu, Capillary-force-assisted clean-stamp transfer of two-dimensional materials, Nano Lett. 17 (11) (2017) 6961–6967, https://doi.org/10.1021/acs.nanolett.7b0344910.1021/acs.nanolett.7b03449.s00110.1021/acs.nanolett.7b03449.s00210.1021/acs.nanolett.7b03449.s003.
[47] J.C. Gu, P. Xiao, J.W. Zhang, Y.J. Huang, T. Chen, Controlled functionalization of carbon nanotubes as superhydrophobic materials for adjustable oil/Water separation, J. Mater. Chem. A 3 (2015) 4124–4128, https://doi.org/10.1039/C4TA07173E.
[48] J. Yang, G.-S. Lin, C.-Y. Mou, K.-L. Tung, Mesoporous silica thin membrane with tunable pore size for ultrahigh permeation and precise molecular separation, ACS Appl. Mater. Interfaces 12 (6) (2020) 7459–7465, https://doi.org/10.1021/acsami.9b2104210.1021/acsami.9b21042.s001.
[49] P.C. Nalam, A. Sheehan, M. Han, R.M. Espinosa-Marzal, Effects of nanoscale roughness on the lubricious behavior of an ionic liquid, Adv. Mater. Interfaces 7 (17) (2020) 2000314, https://doi.org/10.1002/admi.v7.1710.1002/admi.202000314.
[50] G. Hummer, J.C. Rasaiah, J.P. Noworyta, Water conduction through the hydrophobic channel of a carbon nanotube, Nature 414 (6860) (2001) 188–190, https://doi.org/10.1038/35102535.
[51] Y.S. Tu, R.H. Zhou, H.P. Fang, Signal transmission, conversion and multiplication by polar molecules confined in nanochannels, Nanoscale 2 (2010) 1976–1983, https://doi.org/10.1039/C0NR00304B.
[52] S. Wu, K.J. Brzozowski, Surface free energy and polarity of organic pigments, J. Colloid Interface Sci. 37 (4) (1971) 686–690, https://doi.org/10.1016/0021-9797(71)90347-X.
[53] M. Zenkiewicz, New method of analysis of the surface free energy of polymeric materials calculated with Owens-Wendt and Neumann methods, Polimery 51 (51) (2006) 584–587. https://www.researchgate.net/publication/40804787.
[54] X.C. Zhou, Z.X. Wang, R.Z. Epsztein, C. Zhan, W.L. Li, J.D. Fortner, T.A. Pham, J. H. Kim, M. Elimelech, Intrapore energy barriers govern ion transport and selectivity of desalination membranes, Sci. Adv. 6 (2020) 9045, https://doi.org/10.1126/sciadv.abd9045.
[55] G. Yang, Z. Xie, M. Cran, D. Ng, C.D. Easton, M. Ding, H. Xu, S. Gray, Functionalizing graphene oxide framework membranes with sulfonic acid groups for superior aqueous mixture separation, J. Mater. Chem. A 7 (34) (2019) 19682–19690, https://doi.org/10.1039/C9TA04031E.
[56] Y.H. Li, Z.W. Li, F. Aydin, J. Quan, X. Chen, Y.C. Yao, C. Zhan, Y.F. Chen, T. A. Pham, A. Noy, Water-ion permselectivity of narrow-diameter carbon nanotubes, Sci. Adv. 6 (2020) 9966, https://doi.org/10.1126/sciadv.aba9966.

[57] Y. Kang, Y. Xia, H. Wang, X. Zhang, 2D Laminar membranes for selective water and ion transport, Adv. Funct. Mater. 29 (29) (2019) 1902014, https://doi.org/10.1002/adfm.v29.2910.1002/adfm.201902014.
[58] B. Mi, Graphene oxide membranes for ionic and molecular sieving, Science 343 (6172) (2014) 740–742.
[59] G. Liu, W. Jin, Graphene oxide membrane for molecular separation: challenges and opportunities用于分子分离的氧化石墨烯膜: 机遇与挑战, Sci China Mater 61 (8) (2018) 1021–1026, https://doi.org/10.1007/s40843-018-9276-8.
[60] H.-C. Yang, Y. Xie, J. Hou, A.K. Cheetham, V. Chen, S.B. Darling, Janus membranes: creating asymmetry for energy efficiency, Adv. Mater. 30 (43) (2018) 1801495, https://doi.org/10.1002/adma.v30.4310.1002/adma.201801495.